



High-energy long-cycling all-solid-state lithium metal batteries enabled by silver–carbon composite anodes

Yong-Gun Lee¹✉, Satoshi Fujiki¹, Changhoon Jung¹, Naoki Suzuki², Nobuyoshi Yashiro², Ryo Omoda², Dong-Su Ko¹, Tomoyuki Shiratsuchi², Toshinori Sugimoto¹, Saebom Ryu¹, Jun Hwan Ku¹, Taku Watanabe¹, Youngsin Park¹, Yuichi Aihara¹✉, Dongmin Im¹✉ and In Taek Han¹

An all-solid-state battery with a lithium metal anode is a strong candidate for surpassing conventional lithium-ion battery capabilities. However, undesirable Li dendrite growth and low Coulombic efficiency impede their practical application. Here we report that a high-performance all-solid-state lithium metal battery with a sulfide electrolyte is enabled by a Ag-C composite anode with no excess Li. We show that the thin Ag-C layer can effectively regulate Li deposition, which leads to a genuinely long electrochemical cyclability. In our full-cell demonstrations, we employed a high-Ni layered oxide cathode with a high specific capacity ($>210 \text{ mAh g}^{-1}$) and high areal capacity ($>6.8 \text{ mAh cm}^{-2}$) and an argyrodite-type sulfide electrolyte. A warm isostatic pressing technique was also introduced to improve the contact between the electrode and the electrolyte. A prototype pouch cell (0.6 Ah) thus prepared exhibited a high energy density ($>900 \text{ Wh l}^{-1}$), stable Coulombic efficiency over 99.8% and long cycle life (1,000 times).

The demand for higher power and energy density in electrified transport has generated a strong interest in all-solid-state batteries (ASSBs)¹, due to their improved energy density and safety characteristics compared to those of existing lithium ion batteries (LIBs)².

Solid electrolytes such as sulfides^{3–5} and oxides^{6–8} are suitable for the preparation of ASSBs with a high energy density. Among them, sulfide solid electrolytes (SSEs) are the most suitable for use in electric vehicle (EV) batteries due to their high Li-ion conductivity ($1\text{--}25 \text{ mS cm}^{-1}$) at room temperature, which is comparable to that of traditional liquid electrolytes^{3–5}. Furthermore, the Li transference number (t_{Li^+}) of SSEs is close to 1, which is much higher than that of liquid electrolytes ($t_{\text{Li}^+} + t_{\text{Li}^+} \approx 0.5$) and is advantageous for preventing Li dendrite growth⁹. Importantly, owing to the soft mechanical properties of SSEs^{10,11}, the electrode and electrolyte layer can be manufactured by a simple pressing process, which eliminates the need for typical high-temperature sintering and so greatly improves processability and enables thin film preparation and large-scale production, and thus SSEs are prime candidates for use in ASSBs. However, environmental challenges associated with the generation of highly toxic H_2S gas due to the reaction of sulfides with moisture during the SSE preparation remain to be addressed¹². Moreover, except for the argyrodite ($\text{Li}_6\text{PS}_5\text{X}$ ($\text{X} = \text{Cl}, \text{Br}, \text{I}$))-type electrolytes that undergo relatively slow reactions at the interface, most sulfide electrolytes tend to decompose rapidly in contact with lithium metal; this poses additional challenges during the SSE preparation^{13–15}.

Among the oxides, the garnet-type Li-ion conducting $\text{Li}_7\text{La}_3\text{Zr}_2\text{O}_{12}$ electrolyte is a potential candidate for use as a solid electrolyte for preparing ASSBs with a high energy density due to its wide electrochemical stability window and excellent lithium metal compatibility^{6–8}. However, the indispensable requirement for

high-temperature sintering in its fabrication process highlights the need for further studies to enable large-scale production.

Li is the most promising anode for obtaining high energy-density ASSBs for EV applications due to its high theoretical capacity ($3,860 \text{ mAh g}^{-1}$) and low electrochemical potential (-3.04 V versus standard hydrogen electrode)^{16–18}, and is most suitable for replacing the widely used graphite anode (theoretical capacity of 372 mAh g^{-1}) of current LIBs. However, the low Coulombic efficiency and volumetric expansion due to Li dendrite growth are serious challenges that contribute to safety issues and a reduction in the cycle life. Additionally, the cell-fabrication process of lithium metal requires high pressures due to its soft nature^{19–21}, which makes its use in ASSBs rather challenging. To circumvent these limitations, an anode-free concept using a current collector alone as the anode was developed^{22–25}, wherein the cathode is the sole source of the Li metal while charging. As excessive Li is not used in this approach, the energy density of the resulting ASSB can be increased to an extremely high value. Furthermore, this approach does not involve handling Li metal foils in the cell assembly process, which contributes to a reduced battery cost. Although several such advances have been made, solutions for the low Li Coulombic efficiency and extensive dendrite growth are yet to be reported.

We report here that an ASSB with an energy density greater than 900 Wh l^{-1} and long cycle life (1,000 times) can be realized by using a SSE and a Li metal-free anode. This ASSB comprises a Ag-C nanocomposite layer as the anode instead of Li metal (Fig. 1a,b). As Ag is soluble in Li and reduces the nucleation energy for the formation of Li (refs. 26–32), it assists the uniform deposition of Li on the current collector, and thereby improves the performance of the ASSB. Carbon has previously been used as a protective layer or as a three-dimensional host for the deposition of Li metal^{26–28,33,34}, however, in this work it plays the role of a separator to keep the SSE layer

¹Samsung Advanced Institute of Technology (SAIT), Samsung Electronics Co., Ltd, Suwon, Korea. ²Samsung R&D Institute Japan, Osaka, Japan.

✉e-mail: yg23.lee@samsung.com; yuichi.aihara@samsung.com; dongmin.im@samsung.com

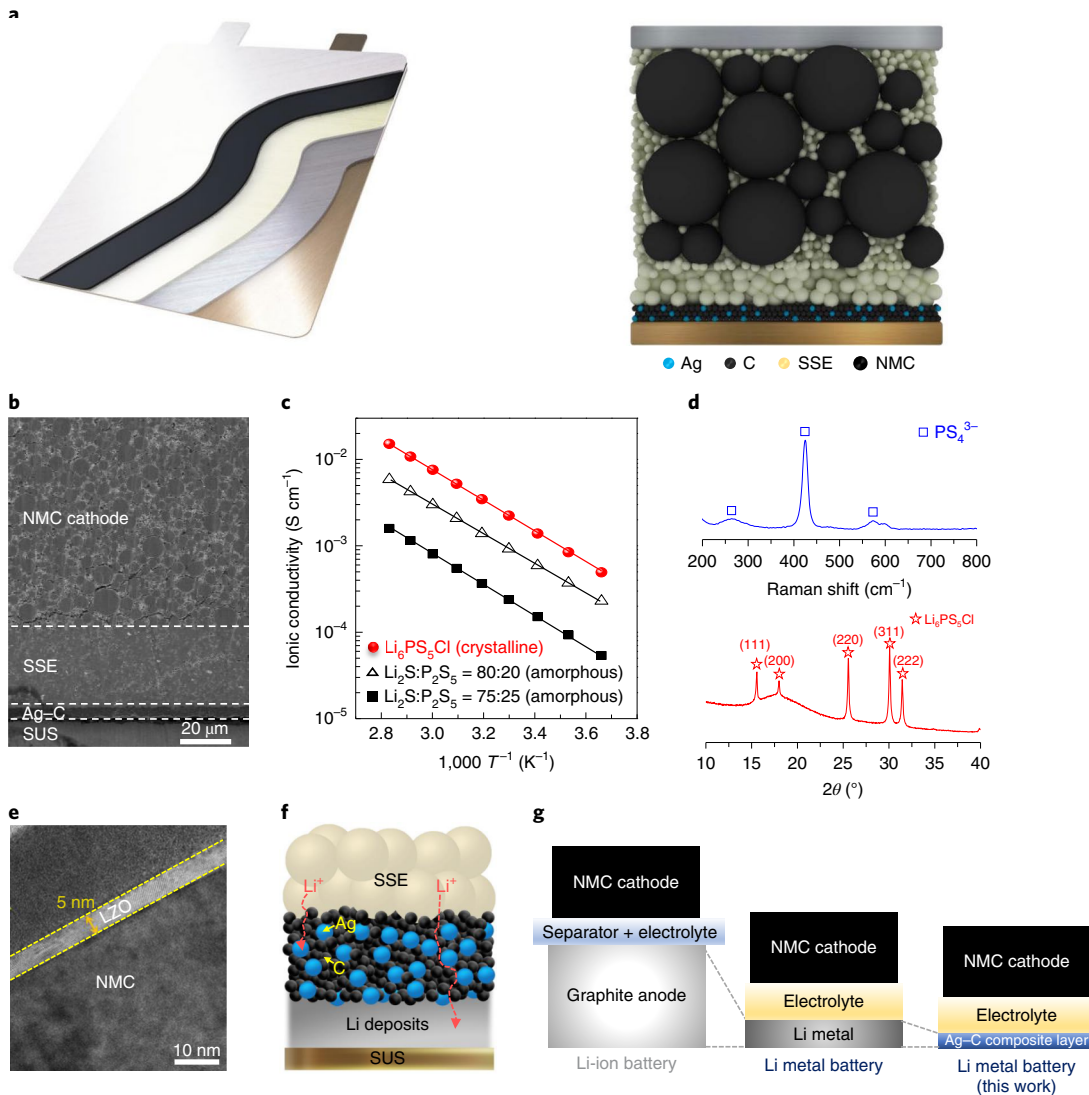


Fig. 1 | All-solid-state lithium metal battery. **a**, Schematic of an ASSB composed of a NMC cathode with a high areal capacity ($>6.8 \text{ mAh cm}^{-2}$), SSE and a Ag-C nanocomposite anode layer that does not require excess Li. Al and SUS foil were used as current collectors for the cathode and anode, respectively. **b**, A cross-sectional SEM image of the ASSB structure shows the intimate contact between the densely integrated components. **c**, Arrhenius plot of SSE ionic conductivities with temperature. **d**, Raman spectrum and XRD pattern of the argyrodite solid electrolyte. **e**, TEM image of an LZO-coated NMC particle. An LZO layer of 5 nm thickness was uniformly coated on the NMC. **f**, Schematic of the Ag-C nanocomposite anode layer on the SUS current collector for stable Li plating and stripping. **g**, Schematic of ASSB that comprises a Ag-C nanocomposite anode layer and exhibits a higher volumetric energy density than those of conventional LIBs and Li metal batteries.

away from Li metal. This improves the durability of SSE and avoids the penetration of Li metal through the SSE.

Construction of the ASSB

Argyrodite-type SSEs have a favourable stability to Li metal in comparison to that of crystalline thio-LiSICON (lithium super ion conductor) and a reasonable ionic conductivity ($>1 \text{ mS cm}^{-1}$), which allows a high cathode loading^{35,36}; due to this, we employed argyrodite ($\text{Li}_6\text{PS}_5\text{Cl}$) as the SSE for our ASSB. The SSE slurry, prepared using argyrodite powder, was coated on a PET film by doctor blading ($t=30 \mu\text{m}$) and was transferred to the $\text{LiNi}_{0.90}\text{Co}_{0.05}\text{Mn}_{0.05}\text{O}_2$ (NMC) cathode by applying external pressure (50 MPa). In LIBs, the separator typically prevents a short-circuit between electrodes. However, we did not use the typical non-woven fabric separator and instead used a film, which was made using a transfer method to improve uniformity and reduce thickness. The soft and elastic

mechanical properties of the argyrodite SSE^{10,11} simplify processing and facilitate an intimate contact between the SSE and the electrodes. The prepared SSE film showed sufficient mechanical strength and flexibility, and its mechanical strength improved further due to an increased density on subjecting it to pressurization through a warm isostatic press (WIP) (Supplementary Fig. 1). To improve the uniformity of the SSE dispersion, which is known to have a significant influence on the mechanical rigidity of the film and its Li-ion conductivity, we prepared the argyrodite slurry in a mixture of xylene and isobutyl isobutyrate (Supplementary Fig. 2). Temperature significantly impacts electrolyte Li-ion conductivity, and Fig. 1c shows the Arrhenius plot of Li-ion conductivities for sulfide electrolytes as a function of temperature. For amorphous sulfide electrolytes, variation in the Li_2S and P_2S_5 composition, such as 75:25 and 80:20, afforded Li-ion conductivities of 0.19 mS cm^{-1} and 0.76 mS cm^{-1} , respectively, at room temperature. In contrast,

crystalline argyrodite showed a higher room-temperature Li-ion conductivity of 1.8 mS cm^{-1} . When a binder was mixed with the SSE, the Li-ion conductivity at room temperature reduced slightly to 1.31 mS cm^{-1} . The activation energy of the prepared SSE was 0.35 eV . Figure 1d shows the Raman spectrum and X-ray diffraction (XRD) pattern of the prepared argyrodite electrolyte. The Raman spectrum showed a peak of around 420 cm^{-1} associated with the PS_4^{3-} ion unit (orthothiophosphate) in argyrodite, and the absence of other peaks in this region indicated the absence of related impurities in the prepared electrolyte. The Raman spectrum of the SSE sheet was almost identical to that of the pristine argyrodite powder, indicative of little chemical or structural change in the argyrodite caused by the solvent or the binder (Supplementary Fig. 3). Further, the XRD pattern indicated that the argyrodite phase exists in the well-formed cubic $F\text{-}43m$ space group, and the peaks at 15, 17, 25, 30 and 31 degrees are related to the (111), (200), (220), (311) and (222) planes, respectively.

We used a NMC cathode with a high areal capacity of 6.8 mAh cm^{-2} in the ASSB to obtain a high energy density ($>900 \text{ Wh l}^{-1}$). However, the interfacial side reactions between the cathode active material and the SSE at high voltages above 4.0 V and the high solid–solid interfacial resistance, which deteriorate ASSBs' capacity and cycle life^{37–39}, are known critical issues with the use of this cathode. Based on our previous results⁴⁰, we applied a 5 nm thick $\text{Li}_2\text{O}\text{-ZrO}_2$ (LZO) coating on the NMC cathode active materials, which can be seen in the transmission electron microscopy (TEM) image (Fig. 1e), to improve the SSE–cathode interfacial properties.

To improve the Li plating and stripping stability during repeated cycling, we introduced a composite anode layer on the stainless steel (SUS) current collector (Fig. 1f), which comprised Ag nanoparticles (NPs) and carbon black in a 1:3 weight ratio, as well as a polyvinylidene fluoride binder. The SUS current collector was chosen due to its high mechanical strength and low reactivity with sulfides (Supplementary Fig. 4). Unlike the ASSBs with a graphite anode, the solid electrolyte is not included inside the anode in our system. Notably, during the charging process, Li metal formed uniformly between the current collector and the Ag–C nanocomposite layer. No metallic Li components were used in the cell assembly, and the Li metal deposited on the SUS current collector, which originated from the cathode, was used as the anode. The implementation of a high Coulombic efficiency and uniform Li deposition without the use of excess Li metal is the key factor to ensure longer lifetimes and the operational safety of ASSBs. As the thickness of the Ag–C nanocomposite layer is only $5\text{--}10 \mu\text{m}$, we were able to accomplish an excellent volumetric cell energy density in the developed ASSB (Fig. 1g).

Li deposition with and without a Ag–C nanocomposite layer

Li metal deposition is greatly affected by the surface properties of the substrate²⁶. To investigate the Li deposition behaviour in the developed ASSB, we first studied this phenomenon when the SUS current collector was used in direct contact with a solid electrolyte in the absence of the additional layer (Fig. 2a). The formation of the Li dendrite was obvious: although the Li deposit ($t=30 \mu\text{m}$) was not dense, it was thick and random- in shape (Fig. 2b,c) although the state of charge (SOC) was only 50% with a 0.05 C rate (0.34 mA cm^{-2}). When the cycle was repeated, the SSE was easily damaged due to the non-homogeneous growth of Li deposits, which increases the probability of short-circuiting. In addition, the discharge capacity decays due to the generation of isolated lithium. Furthermore, the current collector–SSE interface may have insufficient contact due to the formation of microgaps and other side reactions, which result in an uneven Li deposition. Figure 2d shows the cycle performance of a pouch-type full cell ($2 \times 2 \text{ cm}^2$, 20 mAh) using the SUS current collector alone under a $0.1 \text{ C}/0.33 \text{ C}$ charge/discharge rate at 60°C . Indeed, even at some relatively low currents,

the capacity dropped sharply just after a few cycles, which is caused by the non-uniform nucleation and growth of lithium.

In the presence of the Ag–C nanocomposite layer ($5 \mu\text{m}$ thickness), the cross-sectional scanning electron microscopy (SEM) images of the ASSB and energy dispersive spectroscopy (EDS) images of C and Ag (Fig. 3b–d) show that C and Ag are uniformly distributed in the Ag–C nanocomposite layer before charging. After the first charging ($0.1 \text{ C}, 0.68 \text{ mA cm}^{-2}$), dense and uniform Li deposits ($t=25 \mu\text{m}$) formed (Fig. 3c). It is speculated that the application of Ag improves the conductivity and lowers the nucleation energy of Li metal, which results in the uniform Li deposition. The EDS image showed the presence of Ag in the deposited Li metal layer after charging (Fig. 3c). We assume that Ag forms an Ag–Li alloy first in the Ag–C nanocomposite layer, and then part of the Ag moves to the current collector and forms a solid solution with Li metal, and thus facilitates a uniform Li plating. Notably, in the subsequent discharging process, the Li metal layer completely disappears (Fig. 3d), and the lithium passes through the Ag–C and the SSE layers and returns to the cathode. However, the Ag dissolved in the Li layer does not return to the Ag–C nanocomposite layer and remains between the current collector and the Ag–C nanocomposite layer. Figure 3e,f show the distribution of Ag in the Ag–C nanocomposite layer after 1 cycle ($0.1 \text{ C}/0.1 \text{ C}$ charge/discharge rate) and 100 cycles ($0.5 \text{ C}/0.5 \text{ C}$ charge/discharge rate), respectively. Importantly, no residual Li deposits or Li dendrite features were found in the Ag–C nanocomposite layer after these cycles (Supplementary Fig. 5). Although changes in the thickness of the Ag–C nanocomposite layer were negligible, variations in the distribution of Ag in the Ag–C nanocomposite layer were noticeable over the period (100 cycles). The SEM photographs taken at 3 different locations of the ASSB after 1 cycle indicated no significant difference (Fig. 3e). However, the SEM images after 100 cycles indicated that most of Ag NPs existed in the bottom areas near the SUS current collector, and that the particle size had significantly reduced from the initial size (Fig. 3f), which suggests that the Ag in the Ag–C nanocomposite layer continuously moves in the direction of the current collector in each cycle, and does not return to its original position. It is believed that Ag dissolved in Li metal is more energetically favoured than Ag in the nanocomposite layer; however, the specific mechanism of Ag transport needs to be further investigated. Li deposition behaviours with layers of C only and of Ag only were also investigated for comparison (Supplementary Note 1, Supplementary Fig. 6 and Supplementary Table 1).

Morphological variation of the Ag–C nanocomposite layer

We investigated, using SEM, the morphological changes of Ag NPs in the Ag–C nanocomposite layer by varying the cutoff voltage (3.5–4.25 V) during the charging process (Fig. 4). Figure 4a shows the voltage profile and the areal capacities according to the cutoff voltage during charging. The voltage rapidly rose to $\sim 3.55 \text{ V}$ and the slope was subsequently observed to decline drastically. Up to 3.5 V , the shape of the particles did not change significantly; however, an apparent reduction in porosity was distinguished (Fig. 4c). This might be caused by the expansion of the C and Ag particles. The sloping profile is primarily associated with the C lithiation, as confirmed in Supplementary Figs. 6 and 7; further, it is known that the lithiation of amorphous C accompanies the increase in lattice spacing⁴¹. The lithiation of Ag also appears to initiate in this region (Supplementary Fig. 6c). Over the 3.5–3.55 V range, the size of the Ag NPs was observed to increase (Fig. 4d), which indicates the continued lithiation of Ag particles during this period. More drastic changes were observed in the 3.55–3.6 V range, wherein the Ag NPs or Ag–Li alloy NPs began to shrink substantially (Fig. 4e) as plating of the Li metal began on the surface of SUS foil (Fig. 4h). Furthermore, a significant amount of Ag moved from the Ag–C nanocomposite layer to the

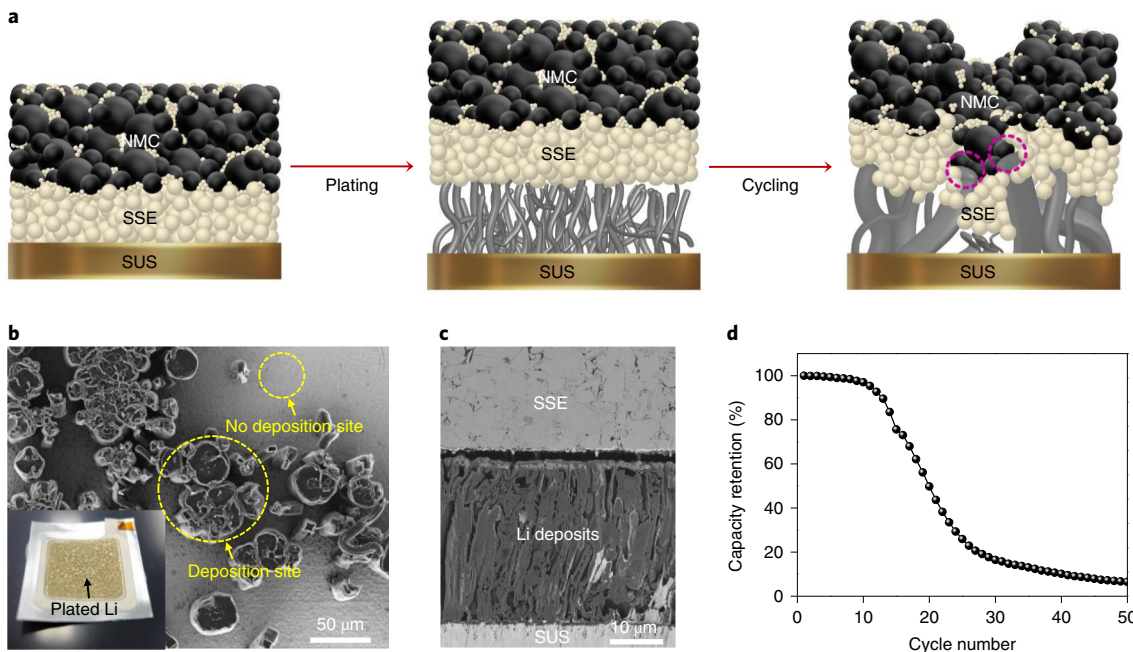


Fig. 2 | Morphology of direct Li plating on the current collector with the SSE. **a**, Schematic of Li plating on the SUS current collector when the current collector is directly assembled with the SSE. **b**, Top view of plated Li after 0.05 C (0.34 mA cm^{-2}) charging and at 50% SOC. Inset: photograph of plated Li on the SUS current collector. **c**, Cross-sectional view of plated Li on the SUS current collector after 0.05 C charging at 100% SOC. **d**, Capacity retention of the SUS|SSE|NMC pouch-type full cell (20 mAh) with a charge/discharge rate of 0.1C/0.33C (voltage window, 2.5–4.25 V versus Li^+/Li at 60 °C).

SUS current collector and dissolved in the plated Li metal, which is in agreement with the SEM-EDS results in Fig. 3c. On further increase, it appeared that the steady state was reached at up to 4.25 V, and no significant changes were observed inside the Ag-C nanocomposite layer (Fig. 4f,g) as the thickness of Li deposit grew continuously until it reached $\sim 25 \mu\text{m}$ (Fig. 4i,j).

The behaviour of the Ag and C particles in the Ag-C nanocomposite layer during cycling was further examined with TEM and electron energy loss spectroscopy (EELS) analyses. In the pristine sample, Ag particles ($\sim 60 \text{ nm}$ particle size) were uniformly distributed and separated from each other, and no network formation was observed (Fig. 5a–c). After the first charging (0.1 C), the Ag NPs became fragmented into smaller ones (Fig. 5d,e). It is reasonable to say that Ag-Li alloys were formed in the course of the charging process, but a large part of the Ag and Li moves to the current collector side at the end of charging, to leave only fragmented particles in the Ag-C nanocomposite layer. In the EELS map (Fig. 5f), the presence of Li in the Ag NPs is not clearly identified, but it was found on the C particles and was observed to not fill the pores between the particles. As Ag NPs are isolated in the matrix of C without connecting to each other and lithium ion is known to diffuse well inside C materials^{42–44}, it is presumed that the C acts as an ion conductor in the nanocomposite layer. After subsequent discharging (0.1 C), when most of the Li has moved back to the cathode side (Fig. 3d), the Ag NPs still remained nanoporous or fragmented (Fig. 5g,h) and the compositional variation was not significant (Fig. 5i). After 100 cycles, the Ag NPs became smaller and sparse (Fig. 5j–l), which implies that the movement of Ag from the Ag-C nanocomposite layer to the anode side is continuous throughout the cycling. However, Ag NPs that were expected to retain their particle size through recrystallization were also observed simultaneously. The crystallinity of Ag and C in the Ag-C nanocomposite layer at various cycle times was analysed by using selected area diffraction patterns (SADP) (Fig. 5m and Supplementary Fig. 8). In the pristine sample, Ag is crystalline and C is amorphous. After the 0.1 C charging process, the

Ag NPs form an Ag-Li alloy, which indicates an amorphous nature. However, some fragmented particles still displayed crystallinity at this stage (Supplementary Fig. 9) and, after subsequent 0.1 C discharging, it was confirmed that the Ag NPs mostly returned to a crystalline form. Additionally, although particle size was reduced, the crystallinity of Ag was retained even after 100 cycles carried out with a high C-rate of 0.5 C/0.5 C.

To further analyse the phase transformation of Ag and the Ag-Li alloy, X-ray diffraction analyses were conducted using Ag-C|SSE|NMC pouch-type full cell (Fig. 5n). In the TEM analysis, the Ag-Li alloy phenomenon cannot be observed accurately because of the self-discharge or damage caused by the electron-beam exposure. Before charging, Ag peaks were observed at 38.2 and 44.3° (ref. ³⁰). After 0.1 C charging, new peaks appeared at 23, 27 and 28.3°, which indicated the formation of a new intermetallic phase, such as Li_3Ag_4 (γ_3) (refs. ^{29,30}). Also, the existing Ag peaks shifted or disappeared. In the subsequent discharging, the peaks of the alloy phase disappeared due to the migration of Li, and the peaks of Ag at 38.4 and 44.6° reappeared after recrystallization.

Overall, Ag NPs form Ag-Li alloys in the early stage of charging, but part of the Ag moves to the current collector, which helps the nucleation of Li metal, which eventually dissolves in the Li deposit at the end of charging. Although there is not clear evidence that confirms the involvement of C in the electrochemical reactions, it is obvious that the C particles conduct Li ions and also mechanically support the Ag-C nanocomposite layer owing to their strong modulus of $\sim 200 \text{ GPa}$ (ref. ⁴⁵).

Pouch cell performance

We developed Ah class ASSB prototypes for EV applications and evaluated their electrochemical performances. A Ag-C nanocomposite layer was introduced to show its performance with the SSE and the high-capacity NMC cathode (6.8 mAh cm^{-2} areal loading) in the 0.6 Ah pouch-type full cell (active area, $6.7 \times 11.2 \text{ cm}^2$), as shown in Fig. 6a. The pouch cell was fabricated by adopting a

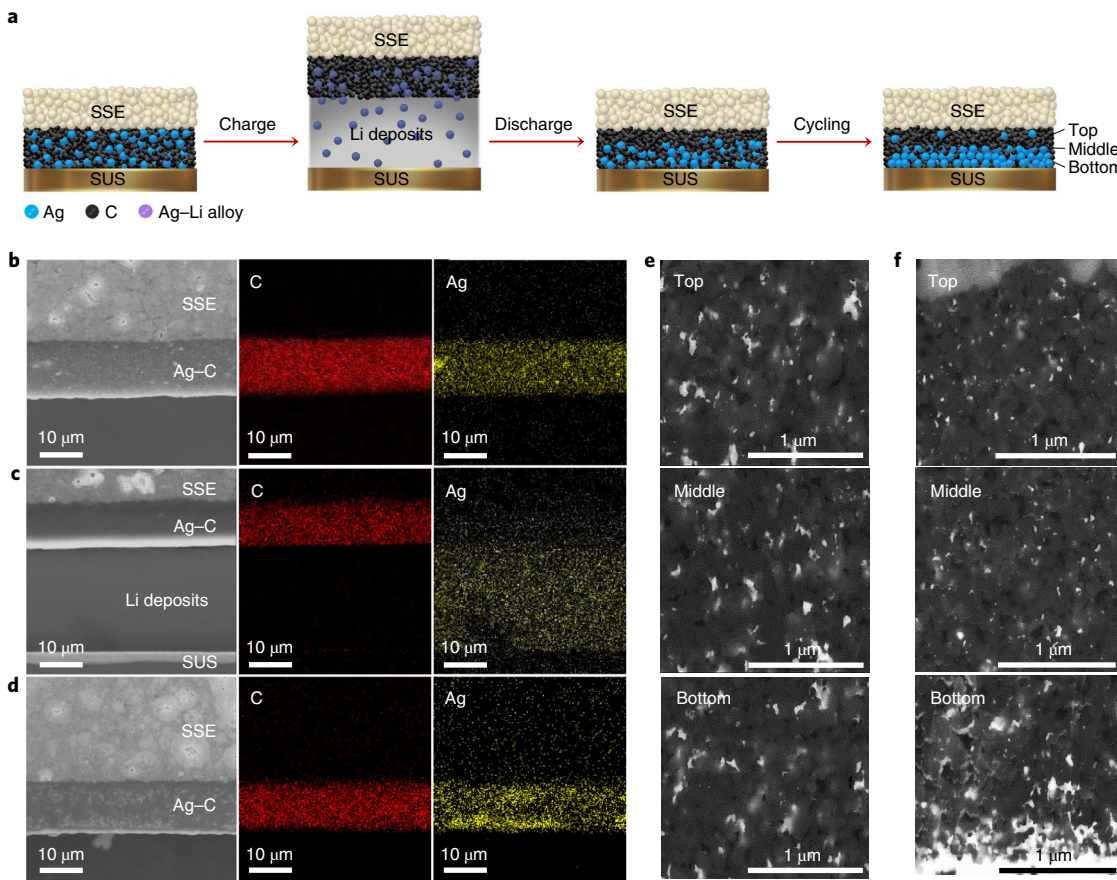


Fig. 3 | Stable Li plating and stripping through the Ag-C nanocomposite layer. **a**, Schematic of Li plating-stripping on the current collector with a Ag-C nanocomposite layer during charging and discharging processes. **b-d**, Cross-sectional SEM and corresponding EDS images for the Ag-C nanocomposite layer. Pristine (**b**), after 0.1C (0.68 mA cm^{-2}) charging (**c**) and after 0.1C (0.68 mA cm^{-2}) discharging (voltage window, 2.5–4.25 V versus Li^+/Li at 60°C) (**d**). **e,f**, Distribution of Ag in the Ag-C nanocomposite layer after 1 cycle (**e**) and 100 cycles (**f**). Cracks or empty spaces below the Ag-C nanocomposite layer were formed during the sample preparation.

bi-cell structure, in which two anodes were placed around a double-sided NMC cathode (Fig. 6a). The internal structure of the bi-cell was examined by X-ray computed tomography (CT) (Fig. 6b). The analysis confirmed that the NMC cathode ($120 \mu\text{m}$), SSE and Ag–C nanocomposite layers ($30 \mu\text{m}$ combined) are positioned symmetrically around the Al current collector. However, the Ag–C and SSE layers are not distinguishable in the X-ray CT image. The analysis also confirmed the intimate contacts at the current collector/electrode interface and the electrode/electrolyte interface. In typical sulfide ASSBs, improvement of the solid–solid interface characteristics along with the micropore challenges and the contact loss problems at the cathode are important issues that need to be addressed^{5,37–39}. Therefore, external pressurization is essential for a uniform interface formation and stable lithium deposition in ASSBs^{11,46}. Particularly, pressurization is unavoidable for high-current operations owing to the inferior interfacial properties in typical ASSBs. To address this problem in the construction of our ASSB, we introduced a WIP cell fabrication process and applied 490 MPa pressure (Fig. 6c). We also applied a uniform pressure of $2\text{--}4 \text{ MPa}$ to the pouch cell using a lab-made pressure jig during the cell operation (Fig. 6c). Our investigations of the influence of WIP and the external pressure are further described in Supplementary Note 2, Supplementary Figs. 10–12 and Supplementary Table 2.

The voltage profiles of the 0.6 Ah pouch-type full cell with the optimized Ag–C nanocomposite layer (Ag:C = 1:3 weight ratio)

(Supplementary Note 3 and Supplementary Figs. 13 and 14) were examined according to cell capacity and specific capacity (Fig. 6d,e). The rate capability by varying the discharge rate from 0.2 C (1.36 mA cm^{-2}) to 2.0 C (13.6 mA cm^{-2}) was examined over the range $2.5\text{--}4.25 \text{ V}$ at a fixed charge rate of 0.1 C (0.68 mA cm^{-2}) in a constant current (CC)–constant voltage (CV) mode. The rate capability ($Q_{1.0\text{C}}/Q_{0.2\text{C}}$) was 93%, and the specific discharge capacity of cathode material at 0.2 C was 215 mAh g^{-1} . In addition, the utilization of more than 80% at a high current density (2.0 C) was obtained (inset of Fig. 6e).

Given the criticality of the operating temperature in EV batteries, we investigated the effect of temperature on voltage profiles and interfacial resistances of ASSBs (Fig. 6f and Supplementary Fig. 15). As the temperature decreased, the resistance increased, and the discharge capacity decreased accordingly. The discharge capacity at 45°C (99.5%) was comparable to that attained at 60°C , and the discharge capacity at 25°C decreased to 90.7%. Encouragingly, more than 40% of the capacity was still exhibited at -10°C . We believe that the low-temperature performance of the ASSBs can be further improved by further lowering the interfacial resistance and increasing the ion conductivity of the solid electrolyte.

The charge-discharge curves for a 0.6 Ah pouch-type full cell at a $0.5 \text{ C}/0.5 \text{ C}$ charge/discharge rate (Supplementary Fig. 16) indicate that the average cell voltage was approximately 3.76 V , and the discharge capacity was 146 mAh g^{-1} , which is 70% of the discharge capacity at 0.2 C (210 mAh g^{-1}). Importantly, the discharge capacity

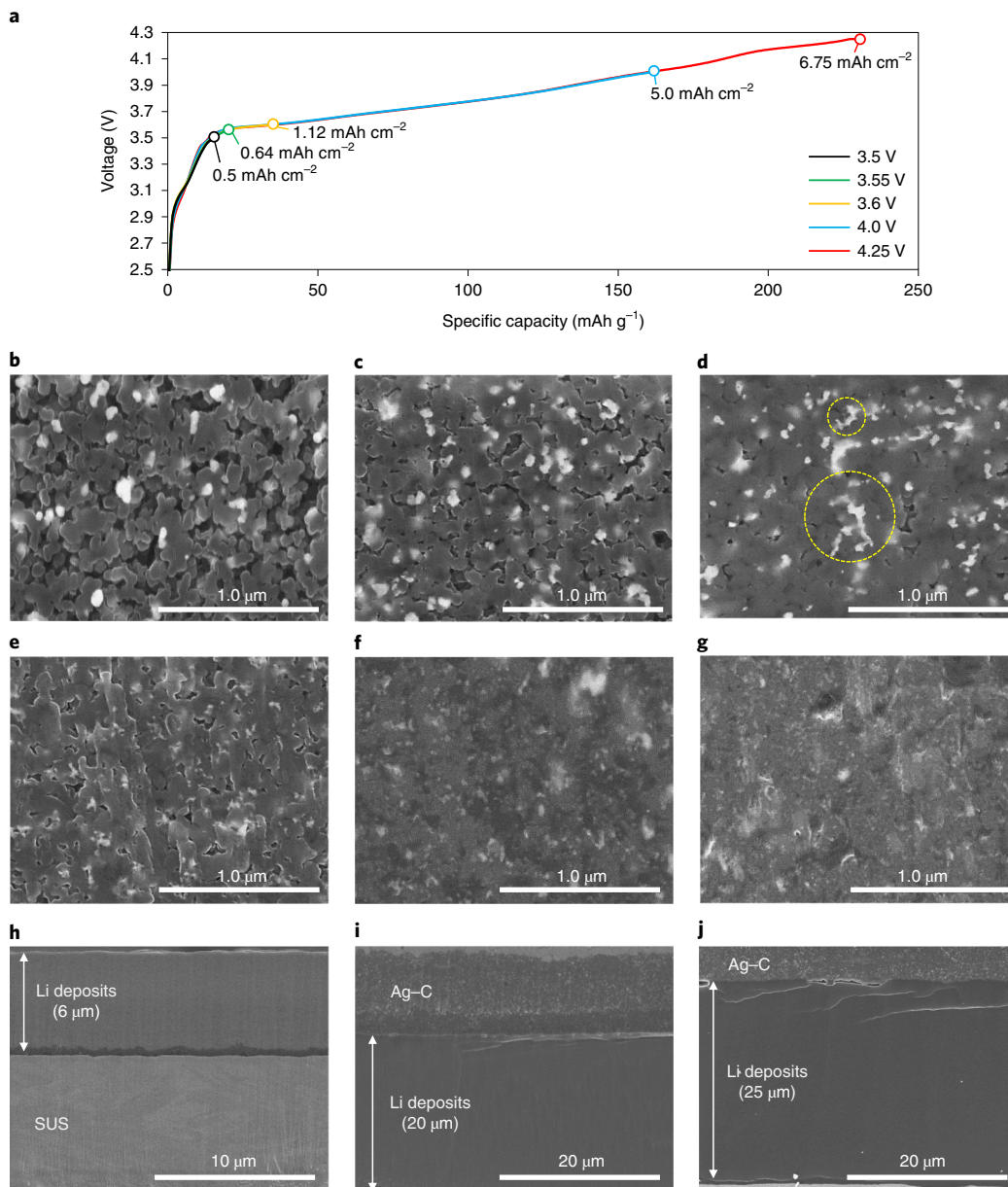


Fig. 4 | Morphological variation of the Ag–C nanocomposite layer. Morphological changes of the Ag NPs in the Ag–C nanocomposite layer during the charging process was monitored by SEM as a function of cutoff voltage. **a**, Voltage profiles with cutoff voltages during a 0.1 C (0.68 mA cm^{-2}) charging. **b–g**, Cross-sectional SEM images of the middle part of the Ag–C nanocomposite layer when pristine (**b**), at 3.5 V (**c**), 3.55 V (**d**), 3.6 V (**e**), 4.0 V (**f**) and 4.25 V (**g**). **h–j**, Cross-sectional SEM images of plated Li at 3.6 V (**h**), 4.0 V (**i**) and 4.25 V (**j**).

was maintained without significant decline over a long cycle and remained at 95% and 89% after 600 and 1,000 cycles, respectively. Cycle performance and the corresponding Coulombic efficiency of the ASSB (Fig. 6g) indicate that the ASSB with a Ag–C nanocomposite layer exhibits superior cycling performance compared to that with the current collector alone as the anode (Fig. 2d). Notably, the ASSB also showed a Coulombic efficiency greater than 99.8%, which is attributed to the robust protection of the NMC cathode by the LZO coating and the stable Li plating, as well as to the stripping between the Ag–C nanocomposite layer and the SUS current collector during the repetitive cell-cycling operation.

The stacking process during the construction of ASSBs is known to be vital for their performance. We analysed this through the cell capacity and energy density with respect to the number of cell stacks (Supplementary Fig. 17 and Supplementary Table 3).

Based on the bi-cell (stack no. = 1), the energy density of 700 Wh l^{-1} was calculated by considering the packaging with a laminate film ($t = 120 \mu\text{m}$). With the current prototype cell structure, it is possible to design an energy density of $>1,000 \text{ Wh l}^{-1}$ by increasing the number of cell stacks and cell area. We constructed $>5 \text{ Ah}$ class prototype cell using multistacking and verified the possibility of its operation (Supplementary Fig. 18). The cell consisted of ten parallel stacks of the bi-cells and was operated under a 0.05 C (0.34 mA cm^{-2})/0.05 C (0.34 mA cm^{-2}) charge/discharge rate without external pressure. Notably, we were able to obtain a discharge capacity of $5,870 \text{ mAh}$ and a high energy density of 942 Wh l^{-1} at 100% SOC with this stacked cell. We also conducted a series of heating and cutting tests (Supplementary Note 4, Supplementary Fig. 19 and Supplementary Videos 1–3), which confirmed the high safety of the ASSBs based on the SSE.

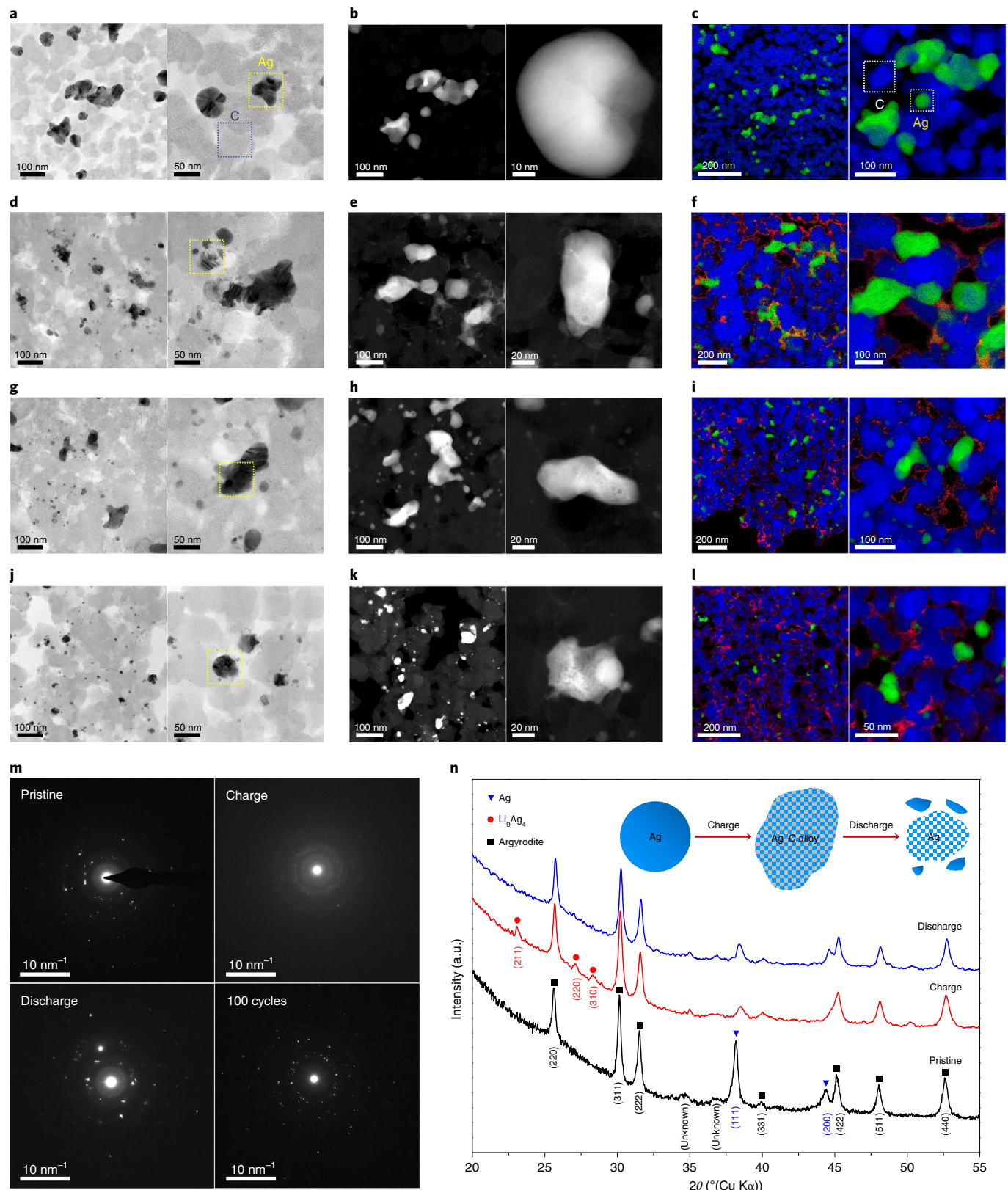


Fig. 5 | Characterization of Ag and C particles in the Ag–C nanocomposite layer after cycling. **a–l**, The Ag–C nanocomposite layer was characterized by TEM and the corresponding EELS mapping. Pristine (**a–c**), after 0.1C charging (**d–f**), after 1 cycle (0.1C/0.1C charge/discharge) (**g–i**) and after 100 cycles (0.5C/0.5C charge/discharge) (**j–l**). Bright-field TEM (**a,d,g,j**), high-angle annular dark field (**b,e,h,k**) and EELS maps of Ag (green), C (blue) and Li (red) (**c,f,i,l**). **m**, Selected area diffraction patterns of Ag NPs in a Ag–C nanocomposite layer during cycling. **n**, X-ray diffraction patterns of the ASSB identify the phase transformation of the Ag–Li alloy. a.u., arbitrary units.

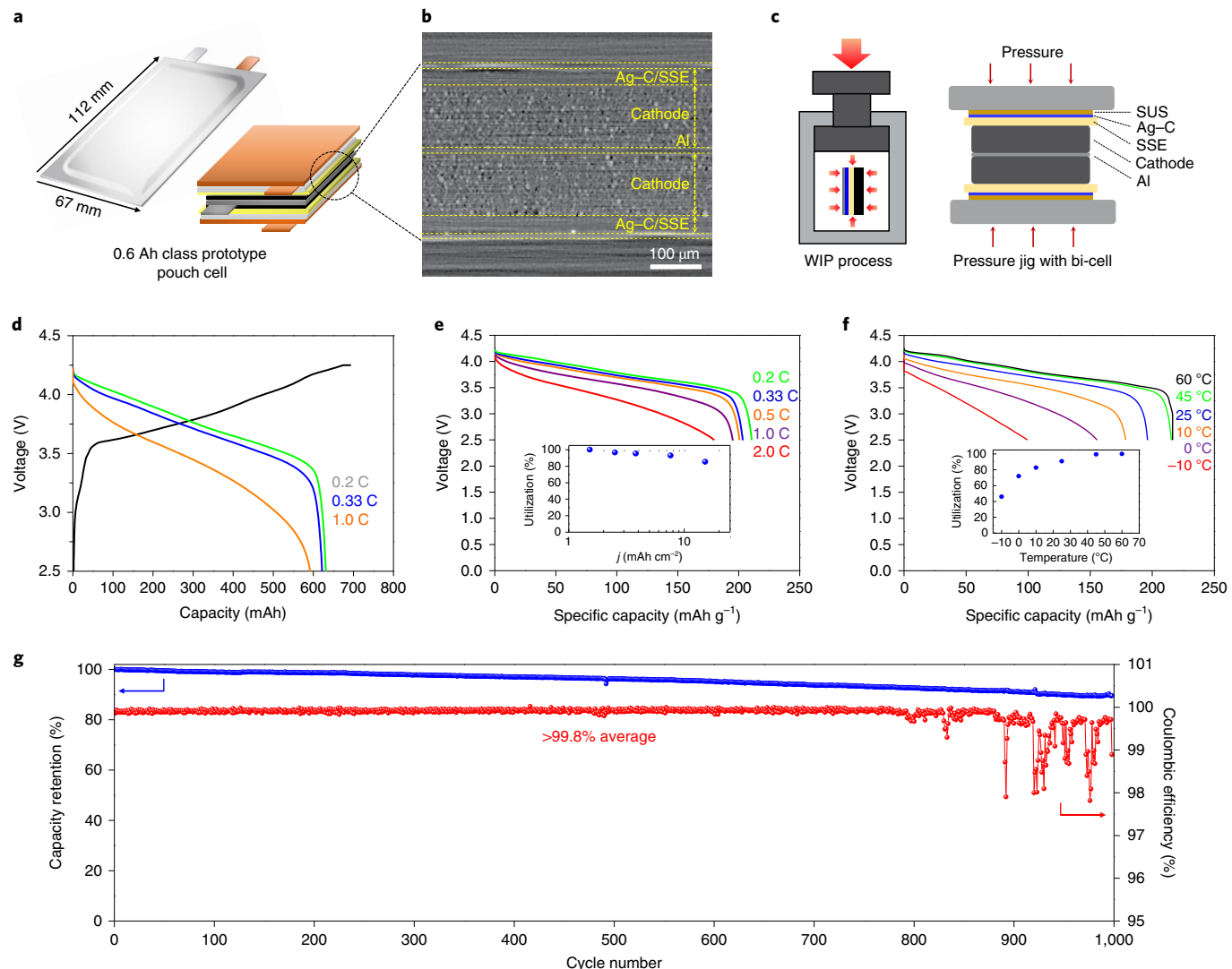


Fig. 6 | Electrochemical performance of ASSB with SSEs. **a**, Characterization of a 0.6 Ah class prototype pouch cell and illustration of a bi-cell structure. **b**, X-ray CT of the bi-cell and symmetric structure based on an aluminium current collector. **c**, Schematic of pressurization process during the fabrication and operation of ASSB. After the cell assembly and stacking, pressurization was applied by using the WIP. During operation, an external pressure of 2 MPa was uniformly applied to the prototype pouch cell using a pressure jig. **d,e**, Rate capability of ASSBs at 60 °C. A 0.1C constant current and 4.25 V constant voltage (CC–CV) mode was adopted for all the charging sequences. Voltage profiles were plotted with cell capacity (**d**) and specific capacity (**e**). **f**, Discharge capacities were monitored under 0.1C/0.1C charge/discharge conditions as the discharging temperature was varied from 60 to –10 °C. The charging temperature was fixed at 60 °C. **g**, Cycling performance and Coulombic efficiency of the Ag–C|SSE|NMC prototype pouch cell (0.6 Ah) are plotted against the cycle numbers. A CC mode with the charge/discharge rate of 0.5 C/0.5 C was applied (voltage window, 2.5–4.25 V versus Li⁺/Li at 60 °C). The areal capacity loading of the NMC cathode was 6.8 mAh cm⁻² (1.0 C = 6.8 mA cm⁻²).

Conclusions

We prepared all-solid-state lithium metal batteries with a high-Ni NMC cathode, an SSE and a Ag–C nanocomposite layer as the anode with the absence of a Li metal foil. The formation of a dense Li metal layer, which could be moved repeatedly between the Ag–C nanocomposite layer and the SUS current collector was demonstrated. Ag NPs were alloyed with Li in the early stage of the charging process, but a significant fraction of Ag was found to move to the current collector side and assist the uniform and dendrite-free plating of Li metal. Notably, the Ah class pouch cells exhibited a high energy density (>900 Wh l⁻¹) and superior cycle life (>1,000 times) which makes this work an important breakthrough in lithium metal battery technology, with potential for future development of EV batteries with a high energy density and safety.

Methods

Preparation of NMC cathode. For the cathode active materials, LZO-coated NMC was prepared by the sol-gel method. The LZO coating solution was prepared from anhydrous 2-propanol, lithium methoxide (10% lithium methoxide in a methanol solution) and zirconium(IV) tetrapropoxide in a 200:20:1 mole ratio. NMC was dispersed in the above solution and stirred for 1 h; subsequently, the propanol was evaporated under vacuum at 50 °C in a water bath, with continuous sonication to prevent the aggregation of the NMC particles. After filtration, the precursor was heated at 300 °C for 1 h in the presence of air to obtain the LZO-coated NMC. The composite cathode was fabricated by mixing LZO-coated NMC, SSE (<1 μm, Mitsui Mining & Smelting Co., Ltd), carbon nanofibres and polytetrafluoroethylene binder (Dupont) (85:15:3:1.5 by weight) in dehydrated xylene (FUJIFILM Wako Pure Chemical Corporation). SSE particles of submicrometre size were employed to increase the contact area and the cathode density. Although there could be more side reactions with smaller SSE particles⁴⁷, the negative influence was not significant under our experimental conditions. The cathode sheet was prepared by the dry film process^{40,48,49}. The

thickness of the cathode sheet was approximately 100 µm and the loading level of the NMC cathode was 6.8 mAh cm⁻². All the processes were carried out in a dry room (dew point below -50 °C).

Preparation of the Ag–C nanocomposite layer. Ag NPs (D50 = 60 nm) and carbon black powder (D50 = 35 nm) were prepared as the anode active materials^{49,50}. Ag and carbon black powder were mixed in a weight ratio of 1:3 in *N*-methylpyrrolidone (Sigma-Aldrich), which containing 7 wt% of polyvinylidene fluoride (Kureha). *N*-methylpyrrolidone was slowly added to the mixture under constant stirring using a mixer (Thinky Corporation, AR-100) to prepare the anode slurry. The slurry was then coated on a 10 µm thick SUS foil using a screen printer and dried in air at 80 °C for 20 min. The obtained electrode was further dried under vacuum at 100 °C for 12 h. The thickness of the Ag–C nanocomposite layer was 5–10 µm. Ag occupied approximately 8 vol% of the composite; the amount of Ag employed in the cell preparation was 8–16 mg Ah⁻¹.

Preparation of SSE sheets. The Li₆PS₅Cl solid electrolyte (99 wt%, 3 µm, Mitsui Mining & Smelting Co., Ltd) and a non-aqueous acrylate-type binder (1 wt%) in xylene (superdehydrated, FUJIFILM Wako Pure Chemical Corporation) and anhydrous isobutyl isobutyrate (Aldrich, 98%) (50:50 w/w) were mixed with 4 Å molecular sieves and ZrO₂ beads (Nikkato, diameter of 3 mm) by using a planetary centrifugal mixer (Thinky Corporation, AR-100) at 2,000 r.p.m. for 6 min (six rotations per minute). The resulting mixture was coated on a release polyethylene terephthalate film (75 µm) using a doctor blade and then the film was dried on a hotplate at 50 °C for a few minutes and dried in a vacuum oven at 40 °C overnight. The thickness of the prepared SSE sheet was ~40 µm, which reduced further to 30 µm after pressurization in a cell. All the processes were carried out in a dry room (dew point below -50 °C).

Fabrication of a pouch-type full cell. A 67 mm × 112 mm bi-cell-type pouch cell with a capacity of 0.6 Ah was fabricated. The electrodes and solid electrolyte sheets were cut using a punching machine. The dimensions of the anode, cathode, and solid electrolyte sheets were 55 mm × 90 mm, 53 mm × 88 mm and 57 mm × 92 mm, respectively. All the electrodes and the electrolyte sheet were stacked and packed into a laminate bag. After applying vacuum to the laminate bag, it was sealed and the cell was pressurized at 490 MPa by the WIP (Sr. CIP, Kobelco). After the press, the cell was removed from the laminate bag and the Al and Ni terminals of the cathode and anode, respectively, were welded using an ultrasonic welder (Branson, 2000X). The cell was then packed into a laminate bag and vacuum sealed again. Most of the assembly process was performed under a dry air atmosphere, in which the dew point was controlled to below -50 °C. Only the isostatic press was performed under ambient atmosphere due to facility limitations.

XRD and Raman spectroscopy. To confirm the crystalline structure of Li₆PS₅Cl solid electrolyte, XRD patterns of the sample were obtained (Bruker, D8 Advance) with a Cu Kα radiation ($\lambda = 1.542 \text{ \AA}$) at room temperature. The sample was then sealed with a polyimide thin film to avoid exposure to air. The Raman spectra were acquired using a micro-Raman spectrometer (Renishaw, inVia) equipped with a 514 nm Ar ion laser. The Li₆PS₅Cl solid electrolyte sample was placed between two glass slides and sealed with epoxy for the Raman analysis under ambient conditions.

X-ray CT. The internal structure of the pouch cell was characterized by X-ray CT (Xradia 520 Versa 3D X-ray microscope, Zeiss). The sample was non-destructively imaged while achieving a high spatial resolution of 820 nm. The generator was operated at 80 kV and 7 W. Three-dimensional datasets were acquired by using the x4 objective lens in combination with the detector, which was set to 2 × 2 binning. To obtain a good signal-to-noise ratio, 3,200 projections were collected with an exposure time of 25 s.

SEM and TEM characterization. The morphologies of the Li deposition and the Ag–C nanocomposite layer were observed using a field-emission scanning electron microscope (SU-8030, Hitachi). Elemental mapping was conducted with an energy dispersive X-ray spectroscope (X-max 80, Oxford). TEM samples were prepared by a focused ion beam system (Helios Nanolab 450F1, FEI), and the final thinning was performed at 5 kV to remove the surface layer damaged by Ga ions. TEM analysis was conducted by a double-Cs-corrected Titan cubed microscope (FEI) at 300 kV with a Quantum 966 energy filter (Gatan Inc.). To prevent the contamination and reaction from exposure to air, a vacuum transfer TEM holder (Model 648, Gatan Inc.) was employed, and all samples were moved from the focused ion beam transfer vessel to a vacuum transfer TEM holder in an Ar-purged glove box.

Electrochemical measurements. The charge–discharge cycling performance was investigated using a multichannel potentiogalvanostat (TOSCAT-3100, TOYO system) in a temperature-controlled chamber. Pouch cells were cycled once at a charging rate of 0.1 C (0.68 mA cm⁻²) and then at a discharging rate of 0.2 C (1.36 mA cm⁻²) in a voltage range of 2.5–4.25 V for the initial formation. A CV was applied until 0.05 C was achieved at 4.25 V, and 10 min holds were made at both 2.5 and 4.25 V. The CC of 0.5 C (3.4 mA cm⁻²) mode was adopted in a cutoff voltage range from 2.5 to 4.25 V versus Li⁺/Li for the cycle performance tests. For rate capability tests, the cells were cycled between 2.5 and 4.25 V with discharging rates

ranging from 0.2 C (1.36 mA cm⁻²) to 2.0 C (13.6 mA cm⁻²). The charging rate was kept constant at 0.1 C (0.68 mA cm⁻²) during the rate capability tests.

The impedance of the pouch-type full cell was measured by electrochemical impedance spectroscopy using an AutoLab modular potentiostat/galvanostat (Metrohm AG) over a 1 MHz to 0.01 Hz frequency range with an amplitude of 10 mV. Characterization of the Li-ion conductivity of the SSE was computed from the impedance measurement carried out using the same method. A sample pellet of SSE was prepared from powder by using a uniaxial press at 300 MPa in a stainless-steel die (diameter of 13 mm). The weight and thickness of the prepared sample pellets were measured to compute their density. A foil (thickness of 50 µm) was attached on both sides of the sample pellet, and a pressure of 30 MPa was applied to make contact. The prepared sample was set in an in-house test cell, which consisted of a polytetrafluoroethylene body, stainless-steel pins and a small spring. The test cell was mounted and enclosed in an Al-laminate bag to protect against air. The cell was then preheated at 80 °C for 12 h, and the impedance was measured from 80 to -20 °C. From the obtained impedance data, the Li-ion conductivity and activation energy were calculated.

Data availability

All the data generated or analysed during this study are included in this published article and its Supplementary Information files. The data that support the plots within this paper are available from the corresponding authors upon reasonable request.

Received: 25 July 2019; Accepted: 7 February 2020;

Published online: 09 March 2020

References

- Schmuck, R., Wagner, R., Hörpel, G., Placke, T. & Winter, M. Performance and cost of materials for lithium-based rechargeable automotive batteries. *Nat. Energy* **3**, 267–278 (2018).
- Janek, J. & Zeier, W. G. A solid future for battery development. *Nat. Energy* **1**, 16141 (2016).
- Kato, Y. et al. High-power all-solid-state batteries using sulfide superionic conductors. *Nat. Energy* **1**, 16030 (2016).
- Kamaya, N. et al. A lithium superionic conductor. *Nat. Mater.* **10**, 682–686 (2011).
- Lau, J. et al. Sulfide solid electrolytes for lithium battery applications. *Adv. Energy Mater.* **8**, 1800933 (2018).
- Han, X. et al. Negating interfacial impedance in garnet-based solid-state Li metal batteries. *Nat. Mater.* **16**, 572–579 (2017).
- Han, F. et al. High electronic conductivity as the origin of lithium dendrite formation within solid electrolytes. *Nat. Energy* **4**, 187–196 (2019).
- Pfenninger, R., Struzik, M., Garbayo, I., Stilp, E. & Rupp, J. L. M. A low ride on processing temperature for fast lithium conduction in garnet solid-state battery films. *Nat. Energy* **4**, 475–483 (2019).
- Xu, K. Electrolytes and interphases in Li-ion batteries and beyond. *Chem. Rev.* **114**, 11503–11618 (2014).
- Nie, K. et al. Interfaces between cathode and electrolyte in solid state lithium batteries: challenges and perspectives. *Front. Chem.* **6**, 616 (2018).
- Sakuda, A., Hayashi, A. & Tatsumisago, M. Sulfide solid electrolyte with favorable mechanical property for all-solid-state lithium battery. *Sci. Rep.* **3**, 2261 (2013).
- Ohtomo, T., Hayashi, A., Tatsumisago, M. & Kawamoto, K. Suppression of H₂S gas generation from the 75Li₂S·25P₂S₅ glass electrolyte by additives. *J. Mater. Sci.* **48**, 4137–4142 (2013).
- Zhou, L. et al. Solvent-engineered design of argyrodite Li₆PS₅X (X = Cl, Br, I) solid electrolytes with high ionic conductivity. *ACS Energy Lett.* **4**, 265–270 (2019).
- Wenzel, S., Sedlmaier, S. J., Dietrich, C., Zeier, W. G. & Janek, J. Interfacial reactivity and interphase growth of argyrodite solid electrolytes at lithium metal electrodes. *Solid State Ion.* **318**, 102–112 (2018).
- Chen, B., Xu, C., Wang, H. & Zhou, J. Insights into interfacial stability of Li₆PS₅Cl solid electrolytes with buffer layers. *Curr. Appl. Phys.* **19**, 149–154 (2019).
- Liu, J. et al. Pathways for practical high-energy long-cycling lithium metal batteries. *Nat. Energy* **4**, 180–186 (2019).
- Armand, M. & Tarascon, J.-M. Building better batteries. *Nature* **451**, 652–657 (2008).
- Xu, W. et al. Lithium metal anodes for rechargeable batteries. *Energy Environ. Sci.* **7**, 513–537 (2014).
- Ferrese, A. & Newman, J. Mechanical deformation of a lithium-metal anode due to a very stiff separator. *J. Electrochem. Soc.* **161**, A1350–A1359 (2014).
- Masias, A., Felten, N., Garcia-Mendez, R., Wolfenstine, J. & Sakamoto, J. Elastic, plastic, and creep mechanical properties of lithium metal. *J. Mater. Sci.* **54**, 2585–2600 (2019).
- Narayan, S. & Anand, L. A large deformation elastic-viscoplastic model for lithium. *Extreme Mech. Lett.* **24**, 21–29 (2018).
- Qian, J. et al. Anode-free rechargeable lithium metal batteries. *Adv. Funct. Mater.* **26**, 7094–7102 (2016).

23. Genovese, M., Louli, A. J., Weber, R., Hames, S. & Dahn, J. R. Measuring the Coulombic efficiency of lithium metal cycling in anode-free lithium metal batteries. *J. Electrochem. Soc.* **165**, A3321–A3325 (2018).
24. Yang, C.-P., Yin, Y.-X., Zhang, S.-F., Li, N.-W. & Guo, Y.-G. Accommodating lithium into 3D current collectors with a submicron skeleton towards long-life lithium metal anodes. *Nat. Commun.* **6**, 8058 (2015).
25. Weber, R. et al. Long cycle life and dendrite-free lithium morphology in anode-free lithium pouch cells enabled by a dual-salt liquid electrolyte. *Nat. Energy* **4**, 683–689 (2019).
26. Yan, K. et al. Selective deposition and stable encapsulation of lithium through heterogeneous seeded growth. *Nat. Energy* **1**, 16010 (2016).
27. Wang, H. et al. Wrinkled graphene cages as hosts for high-capacity Li metal anodes shown by cryogenic electron microscopy. *Nano Lett.* **19**, 1326–1335 (2019).
28. Yang, C. et al. Ultrafine silver nanoparticles for seeded lithium deposition toward stable lithium metal anode. *Adv. Mater.* **29**, 1702714 (2017).
29. Park, C.-M., Kim, J.-H., Kim, H. & Sohn, H.-J. Li-alloy based anode materials for Li secondary batteries. *Chem. Soc. Rev.* **39**, 3115–3141 (2010).
30. Park, C.-M., Jung, H. & Sohn, H.-J. Electrochemical behaviors and reaction mechanism of nanosilver with lithium. *Electrochim. Solid-State Lett.* **12**, A171–A175 (2009).
31. Feng, W., Dong, X., Li, P., Wang, Y. & Xia, Y. Interfacial modification of Li/garnet electrolyte by a lithophilic and breathing interlayer. *J. Power Sources* **419**, 91–98 (2019).
32. Pei, A., Zheng, G., Shi, F., Li, Y. & Cui, Y. Nanoscale nucleation and growth of electrodeposited lithium metal. *Nano Lett.* **17**, 1132–1139 (2017).
33. Wang, M. et al. Porous carbon hosts for lithium–sulfur batteries. *Chem. Eur. J.* **25**, 3710–3725 (2019).
34. Xie, J. et al. Engineering stable interfaces for three-dimensional lithium metal anodes. *Sci. Adv.* **4**, eaat5168 (2018).
35. Kraft, M. A. et al. Inducing high ionic conductivity in the lithium superionic argyrodites $\text{Li}_{6+x}\text{P}_{1-x}\text{Ge}_x\text{S}_3\text{I}$ for all-solid-state batteries. *J. Am. Chem. Soc.* **140**, 16330–16339 (2018).
36. Kato, Y. et al. All-solid-state batteries with thick electrode configurations. *J. Phys. Chem. Lett.* **9**, 607–613 (2018).
37. Koerver, R. et al. Redox-active cathode interphases in solid-state batteries. *J. Mater. Chem. A* **5**, 22750–22760 (2017).
38. Koerver, R. et al. Capacity fade in solid-state batteries: interphase formation and chemomechanical processes in nickel-rich layered oxide cathodes and lithium thiophosphate solid electrolytes. *Chem. Mater.* **29**, 5574–5582 (2017).
39. Xiao, Y., Miara, L. J., Wang, Y. & Ceder, G. Computational screening of cathode coatings for solid-state batteries. *Joule* **3**, 1252–1275 (2019).
40. Ito, S. et al. A rocking chain type all-solid-state lithium ion battery adopting $\text{Li}_2\text{O}-\text{ZrO}_2$ coated $\text{LiNi}_{0.8}\text{Co}_{0.15}\text{Al}_{0.05}\text{O}_2$ and a sulfide based electrolyte. *J. Power Sources* **248**, 943–950 (2014).
41. Stevens, D. A. & Dahn, J. R. The mechanisms of lithium and sodium insertion in carbon materials. *J. Electrochem. Soc.* **148**, A803–A811 (2001).
42. Dahn, J. R., Zheng, T., Liu, Y. & Xue, J. S. Mechanisms for lithium insertion in carbonaceous materials. *Science* **270**, 590–593 (1995).
43. Tachikawa, H. & Shimizu, A. Diffusion dynamics of the Li atom on amorphous carbon: a direct molecular orbital–molecular dynamics study. *J. Phys. Chem. B* **110**, 20445–20450 (2016).
44. Persson, K. et al. Lithium diffusion in graphitic carbon. *J. Phys. Chem. Lett.* **1**, 1176–1180 (2010).
45. Zheng, G. et al. Interconnected hollow carbon nanospheres for stable lithium metal anodes. *Nat. Nanotechnol.* **9**, 618–623 (2014).
46. Zhang, W. et al. (Electro)chemical expansion during cycling: monitoring the pressure changes in operating solid-state lithium batteries. *J. Mater. Chem. A* **5**, 9929–9936 (2017).
47. Walther, F. et al. Visualization of the interfacial decomposition of composite cathodes in argyrodite-based all-solid-state batteries using time-of-flight secondary-ion mass spectrometry. *Chem. Mater.* **31**, 3745–3755 (2019).
48. Hippauf, F. et al. Overcoming binder limitations of sheet-type solid-state cathodes using a solvent-free dry-film approach. *Energy Storage Mater.* **21**, 390–398 (2019).
49. Suzuki, N., Yashiro, N., Yamada, T. & Aihara, Y. All-solid-state secondary battery and method of charging the same. US patent no. US20190157723A1.
50. Suzuki, N., Yashiro, N. & Aihara, Y. Li electroplating/stripping on the metal substrate coated with carbon black. In: *Proc. 235th ECS Meeting abstr.* 163 (ECS, 2019).

Acknowledgements

This work was supported by funds from Samsung Electronics Co. Ltd.

Author contributions

D.I., Y.A. and I.T.H. proposed and supervised the research. N.S., N.Y. and Y.A. proposed the metal–carbon composite concept. Y.-G.L., T. Sugimoto, S.R., N.S. and N.Y. optimized the Ag–C composite anode as well as the current collectors for the anode to achieve the best cycle performance. J.H.K., S.F. and T. Shiratsuchi optimized the effect of external pressure on the battery performance. R.O. developed and optimized the SSE. S.F. and T. Shiratsuchi designed and fabricated the high-Ni-based NMC cathode and prototype ASSB as well as the stacked cell (<5 Ah). S.F., R.O. and T. Shiratsuchi carried out the safety tests for LIB and ASSB. C.J. and Y.-G.L. conducted the SEM, Raman and XRD characterizations. D.-S.K. performed the TEM characterization to monitor the morphological changes in the Ag and C particles. S.R. and Y.-G.L. performed the X-ray CT analysis. Y.-G.L., T. Sugimoto, J.H.K., S.R., Y.P., S.E., N.S., N.Y., R.O., T. Shiratsuchi and T.W. performed the electrochemical characterizations. Y.-G.L., D.I., Y.A., S.F. and T.W. analysed the data and wrote the manuscript. All the authors discussed the results and commented on the manuscript.

Competing interests

All the authors are employed at Samsung Electronics Co. Ltd.

Additional information

Supplementary information is available for this paper at <https://doi.org/10.1038/s41560-020-0575-z>.

Correspondence and requests for materials should be addressed to Y.-G.L., Y.A. or D.I.

Reprints and permissions information is available at www.nature.com/reprints.

Publisher's note Springer Nature remains neutral with regard to jurisdictional claims in published maps and institutional affiliations.

© The Author(s), under exclusive licence to Springer Nature Limited 2020